Composition Effects of FePt Alloy Nanoparticles on the Electro-Oxidation of Formic Acid

Wei Chen,[†] Jaemin Kim,[‡] Shouheng Sun,[‡] and Shaowei Chen*,[†]

Department of Chemistry and Biochemistry, University of California, 1156 High Street, Santa Cruz, California 95064, and Department of Chemistry, Brown University, Providence, Rhode Island 02912

Received June 5, 2007. In Final Form: August 7, 2007

The catalytic activities of Fe_xPt_{100-x} alloy nanoparticles at different compositions ($x = 10, 15, 42, 54, 58$, and 63) in the electro-oxidation of formic acid have been investigated by using cyclic voltammetry (CV), chronoamperometry, and electrochemical impedance spectroscopy (EIS). It was observed that the electrocatalytic performance was strongly dependent on the FePt particle composition. In chronoamperometric measurements, the alloy particles at $x \approx 50$ showed the highest steady-state current density among the catalysts under study and maintained the best long-term stability. In addition, on the basis of the anodic peak current density, onset potentials, and the ratios of the anodic peak current density to the cathodic peak current density in CV studies, the catalytic activity for HCOOH oxidation was found to decrease in the order of $Fe_{42}Pt_{58} > Fe_{54}Pt_{46} \approx Fe_{58}Pt_{42} > Fe_{15}Pt_{85} > Fe_{10}Pt_{90} > Fe_{63}Pt_{37}$. That is, within the present experimental context, the alloy nanoparticles at $x \approx 50$ appeared to exhibit the maximum electrocatalytic activity and stability with optimal tolerance to CO poisoning. Consistent responses were also observed in electrochemical impedance spectroscopic measurements. For the alloy nanoparticles that showed excellent tolerance to CO poisoning, the impedance in the Nyquist plots was found to change sign from positive to negative with increasing electrode potential, suggesting that the electron-transfer kinetics evolved from resistive to pseudoinductive and then to inductive characters. However, for the nanoparticles that were heavily poisoned by adsorbed CO species during formic acid oxidation, the impedance was found to be confined to the first quadrant at all electrode potentials. The present work highlights the influence of the molecular composition of Pt-based alloy electrocatalysts on the performance of formic acid electro-oxidation, an important aspect in the design of bimetal electrocatalysts in fuel cell applications.

Introduction

Fuel cells have been hailed as an important power source in the future because of the high energy conversion efficiency and low environmental pollution.[1] Up to now, one of the major problems in small molecule (e.g., methanol or formic acid) fuel cells is the poisoning of the electrocatalysts by CO formed during the incomplete oxidation of the organic fuels. To improve the performance in fuel oxidation, the combination of Pt and other transition metals has been examined extensively as effective catalysts for methanol and formic acid electro-oxidation, as Pt-based alloy catalysts typically display enhanced catalytic activity toward methanol and formic acid oxidation that has been attributed to the so-called bifunctional and/or electronic (ligand) effect mechanism.[2−12]

In previous studies of metal nanoparticle catalysts, it has been found that the electrocatalytic activity depends strongly on the particle dimensions and surface morphology because of the variation of the density of active sites such as atomic steps, edges, and kinks.[13−16] For example, a recent report demonstrates that platinum nanoparticles with high-index facets exhibit unusually high catalytic activities in the electro-oxidation of small organic fuels.[16] In another study,[13] the effects of the size of palladium nanoparticles on the electrocatalytic oxidation of formic acid were examined, and it was found that the smallest Pd nanoparticles (9 and 11 nm) exhibited the best catalytic activity within the size range of 9−40 nm. For Pt-based binary alloy catalysts, Pt and the second metal play different roles in the oxidation catalysis. According to the so-called bifunctional mechanism, the role of the second metal is to dissociate water to form adsorbed OH species, which then react with CO adsorbed on the Pt surface to generate CO_2.[17,18] This suggests that for alloy nanoparticle catalysts, in addition to particle dimensions, the composition of the bimetallic particles also acts as a very important parameter to manipulate its catalytic activity. Such

* To whom correspondence should be addressed. E-mail: schen@chemistry.ucsc.edu.
  † University of California.
  ‡ Brown University.

(1) Dillon, R.; Srinivasan, S.; Arico, A. S.; Antonucci, V. *J. Power Sources* **2004**, *127*, 112−126.
(2) Wang, H. S.; Wingender, C.; Baltruschat, H.; Lopez, M.; Reetz, M. T. *J. Electroanal. Chem.* **2001**, *509*, 163−169.
(3) Park, K. W.; Choi, J. H.; Kwon, B. K.; Lee, S. A.; Sung, Y. E.; Ha, H. Y.; Hong, S. A.; Kim, H.; Wieckowski, A. *J. Phys. Chem. B* **2002**, *106*, 1869−1877.
(4) Colmati, F.; Antolini, E.; Gonzalez, E. R. *Electrochim. Acta* **2005**, *50*, 5496−5503.
(5) Antolini, E.; Salgado, J. R. C.; Gonzalez, E. R. *J. Electroanal. Chem.* **2005**, *580*, 145−154.
(6) Motoo, S.; Watanabe, M. *J. Electroanal. Chem.* **1976**, *69*, 429−431.
(7) Roychowdhury, C.; Matsumoto, F.; Zeldovich, V. B.; Warren, S. C.; Mutolo, P. F.; Ballesteros, M.; Wiesner, U.; Abruña, H. D.; DiSalvo, F. J. *Chem. Mater.* **2006**, *18*, 3365−3372.
(8) Jayashree, R. S.; Spendelow, J. S.; Yeom, J.; Rastogi, C.; Shannon, M. A.; Kenis, P. J. A. *Electrochim. Acta* **2005**, *50*, 4674−4682.
(9) Lin, W. F.; Zei, M. S.; Eiswirth, M.; Ertl, G.; Iwasita, T.; Vielstich, W. *J. Phys. Chem. B* **1999**, *103*, 6968−6977.
(10) Frelink, T.; Visscher, W.; vanVeen, J. A. R. *Langmuir* **1996**, *12*, 3702−3708.
(11) Page, T.; Johnson, R.; Hormes, J.; Noding, S.; Rambabu, B. *J. Electroanal. Chem.* **2000**, *485*, 34−41.
(12) Lai, L. B.; Chen, D. H.; Huang, T. C. *J. Mater. Chem.* **2001**, *11*, 1491−1494.
(13) Zhou, W. P.; Lewera, A.; Larsen, R.; Masel, R. I.; Bagus, P. S.; Wieckowski, A. *J. Phys. Chem. B* **2006**, *110*, 13393−13398.
(14) Bergamaski, K.; Pinheiro, A. L. N.; Teixeira-Neto, E.; Nart, F. C. *J. Phys. Chem. B* **2006**, *110*, 19271−19279.
(15) Mayrhofer, K. J. J.; Blizanac, B. B.; Arenz, M.; Stamenkovic, V. R.; Ross, P. N.; Markovic, N. M. *J. Phys. Chem. B* **2005**, *109*, 14433−14440.
(16) Tian, N.; Zhou, Z.-Y.; Sun, S.-G.; Ding, Y.; Wang, Z. L. *Science* **2007**, *316*, 732−735.
(17) Iwasita, T. *Electrochim. Acta* **2002**, *47*, 3663−3674.
(18) Tong, Y. Y.; Kim, H. S.; Babu, P. K.; Waszczuk, P.; Wieckowski, A.; Oldfield, E. *J. Am. Chem. Soc.* **2002**, *124*, 468−473.

composition effects have been observed for CO and methanol electro-oxidation with PtRu alloy catalysts.[6,19−25] It was found that for direct methanol fuel cells (DMFC), the optimum catalyst corresponded to a composition consisting of 1:1 atomic ratio of Ru/Pt.[20,21] Yet, so far, the studies of the influence of the catalyst composition on the electrocatalytic activity have been mostly confined to bulk alloy electrodes. Systematic studies of alloy nanoparticles, however, are still scarce due to the difficulty in the synthesis of alloy nanoparticles of controlled compositions.

In our previous studies,[26,27] $Fe_{20}Pt_{80}$ nanoparticles were found to exhibit very good electrocatalytic activities for formic acid electro-oxidation. In this paper, a series of (almost) monodispersed $Fe_xPt_{100−x}$ alloy nanoparticles with different atomic ratios of Fe to Pt were prepared by a chemical reduction method. The $Fe_xPt_{100−x}$ nanoparticles (average diameter ∼2.5 nm) were deposited onto a gold electrode surface (denoted as $Fe_xPt_{100−x}$/Au), and the electrochemical performance in formic acid oxidation was then examined by voltammetric and electrochemical impedance measurements. The electrocatalytic activities were compared on the basis of (steady-state) current density and tolerance to CO adsorption of formic acid oxidation. It was found that within the present experimental context, the $Fe_xPt_{100−x}$ particles at $x \approx 50$ exhibited the optimal composition for formic acid electro-oxidation.

Experimental Section

Chemicals. Perchloric acid ($HClO_4$, Fisher, 99.999%) and formic acid (HCOOH, ACROS, 99%) were used as received. All solvents were obtained from typical commercial sources at their highest purity and used as received as well. Water was supplied by a Barnstead Nanopure water system (18.3 MΩ·cm).

Nanoparticle Preparation. The synthesis and characterization of the $Fe_xPt_{100−x}$ alloy nanoparticles stabilized by oleylamine and oleic acid have been described previously.[26,28] In a typical experiment, 20 mL of dioctylether or benzyl ether was mixed with 0.5 mmol of Pt(acac)$_2$ and 1.5 mmol of 1,2-hexadecanediol. Under a gentle N_2 flow, the mixture was heated to 100 °C. At this temperature, 0.5 mmol of oleic acid, 0.5 mmol of oleylamine, and 1.0 mmol of Fe-$(CO)_5$ (the composition was varied by the amount of $Fe(CO)_5$, from 0.5 to 2.5 mmol) were added under a N_2 blanket, and the mixture was heated to reflux (297 °C) for 30 min before it was cooled down to room temperature. The product was precipitated by adding ethanol and separated by centrifugation. The supernatant was discarded, and the precipitate was dispersed in hexane. Then, an excess of ethanol was added to precipitate out the particles, and the suspension was centrifuged again. By repeating the dispersion−precipitation cycle, excess free ligands were removed affording purified particle samples.

The size of the FePt nanoparticles was then characterized by transmission electron microscopy (TEM, Philips EM420, 120 kV), and energy-dispersive X-ray analysis (EDX) was carried out to evaluate the particle compositions by using an INCA accessory (from

(19) Wang, Y.; Fachini, E. R.; Cruz, G.; Zhu, Y.; Ishikawa, Y.; Colucci, J. A.; Cabrera, C. R. *J. Electrochem. Soc.* **2001**, *148*, C222−C226.
(20) Watanabe, M.; Uchida, M.; Motoo, S. *J. Electroanal. Chem.* **1987**, *229*, 395−406.
(21) Dinh, H. N.; Ren, X. M.; Garzon, F. H.; Zelenay, P.; Gottesfeld, S. *J. Electroanal. Chem.* **2000**, *491*, 222−233.
(22) Dubau, L.; Coutanceau, C.; Garnier, E.; Leger, J. M.; Lamy, C. *J. Appl. Electrochem.* **2003**, *33*, 419−429.
(23) Iwasita, T.; Hoster, H.; John-Anacker, A.; Lin, W. F.; Vielstich, W. *Langmuir* **2000**, *16*, 522−529.
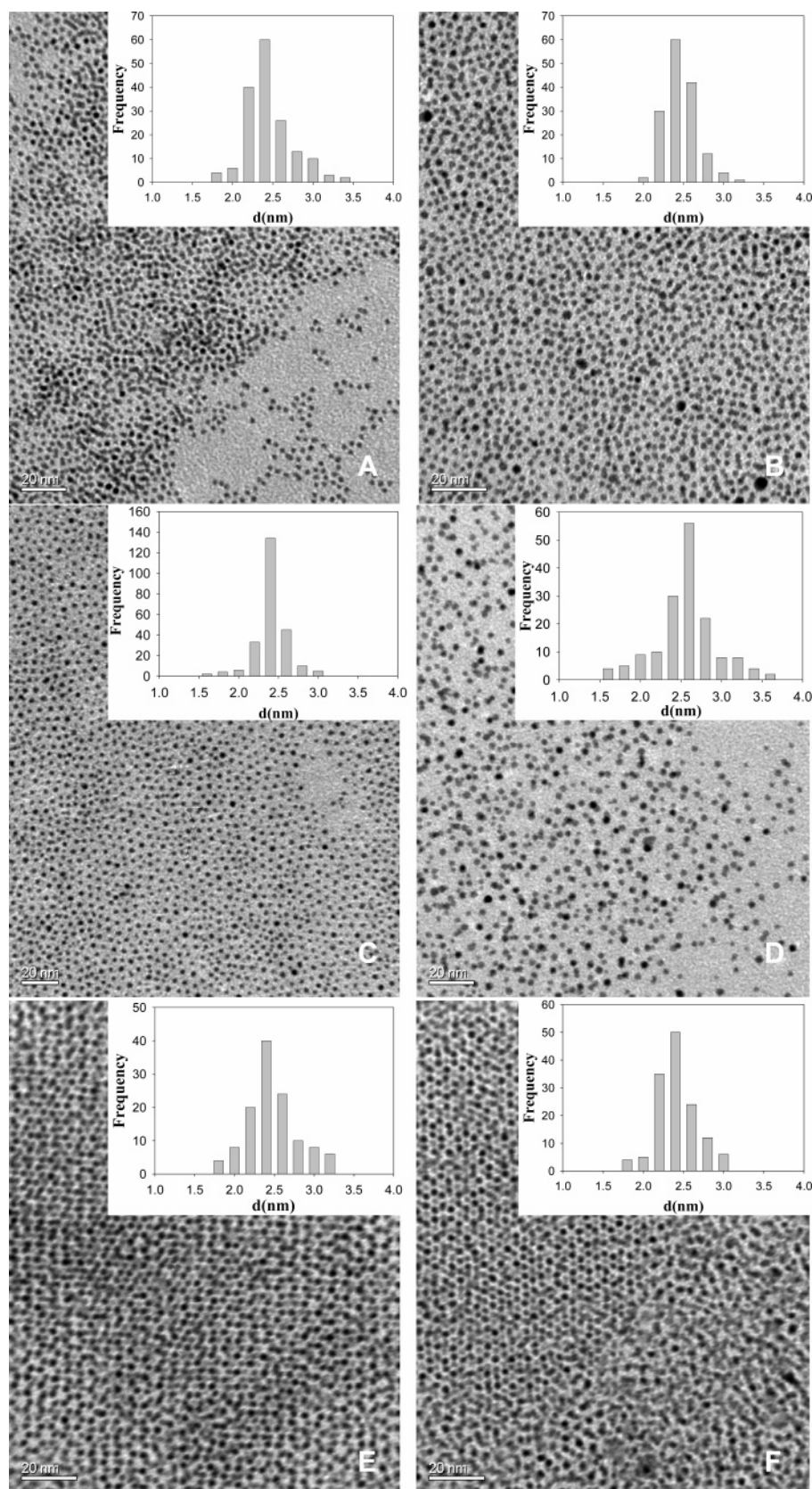(24) Hoster, H.; Iwasita, T.; Baumgartner, H.; Vielstich, W. *Phys. Chem. Chem. Phys.* **2001**, *3*, 337−346.
(25) Shao, Z. G.; Zhu, F. Y.; Lin, W. F.; Christensen, P. A.; Zhang, H. M. *J. Power Sources* **2006**, *161*, 813−819.
(26) Chen, W.; Kim, J.; Sun, S. H.; Chen, S. W. *Phys. Chem. Chem. Phys.* **2006**, *8*, 2779−2786.
(27) Chen, W.; Kim, J.; Xu, L.-P.; Sun, S.; Chen, S. W. *J. Phys. Chem. C* **2007**, *111*, 13452−13459.
(28) Sun, S. H.; Murray, C. B.; Weller, D.; Folks, L.; Moser, A. *Science* **2000**, *287*, 1989−1992.

OXFORD instruments) that was attached onto a scanning electron microscope (SEM, Zeiss (LEO) 1530VP FESEM). UV−vis spectroscopic studies were performed with an ATI Unicam UV4 spectrometer using a 1 cm quartz cuvette with a resolution of 2 nm. The particles were dissolved in dichloromethane at a concentration of ca. 0.1 mg/mL. Only featureless Mie characters were observed in the absorption spectra of these alloy nanoparticles (Supporting Information).

Preparation of the FePt/Au Electrode. The procedure has been described previously.[26] Briefly, a polycrystalline gold disk electrode (sealed in a glass tubing) was first polished with alumina slurries (0.05 μm) and then cleansed by sonication in 0.1 M HNO_3, H_2SO_4, and Nanopure water for 10 min successively. A volume of 4 μL of $Fe_xPt_{100−x}$ nanoparticles dissolved in CH_2Cl_2 (1.2 mg/mL) was then dropcast onto the clean Au electrode surface by a Hamilton microliter syringe. The particle film was dried by a gentle nitrogen flow for ca. 2 min. The organic protecting ligands were then removed by oxidation in an ultraviolet ozone (UVO) chamber (Jelight Company, Inc., model 42) for about 15 min. The particle film was then rinsed with excessive ethanol and Nanopure water to remove loosely bound particles and remaining organic deposits.

Electrochemistry. Voltammetric measurements were carried out with a CHI 440 electrochemical workstation. The $Fe_xPt_{100−x}$/Au electrode was used as the working electrode. A Ag/AgCl wire and a Pt coil were used as the reference and counter electrodes, respectively. All electrode potentials in the present study will be referred to this Ag/AgCl quasi-reference. Electrochemical impedance spectroscopy (EIS) measurements were carried out using an EG&G PARC potentiostat/galvanostat (model 283) and frequency response detector (model 1025). The impedance spectra were recorded between 100 kHz and 10 mHz with the amplitude (rms value) of the ac signal 10 mV. In these voltammetric and impedance measurements, the solutions were deaerated by bubbling ultrahigh-purity N_2 for 20 min and protected with a nitrogen atmosphere during the entire experimental procedure.

Results and Discussion

Characterization of $Fe_xPt_{100−x}$ Nanoparticles. Figure 1 depicts the representative TEM micrographs of the $Fe_xPt_{100−x}$ nanoparticles along with the particle core size histograms as the corresponding insets. It can be seen that the vast majority of the particles exhibit a core diameter close to 2.5 nm with no apparent aggregation, and the core size distributions are all very narrow. The composition of the $Fe_xPt_{100−x}$ nanoparticles was tuned by simply varying the stoichiometic ratio of the Fe and Pt precursors in the synthesis, where the value of x was found to vary from 10 to 63, as estimated from EDX analysis (spectra included in the Supporting Information as Figure S2). Table 1 summarizes the average size, size distribution, and the corresponding composition of the six FePt particle samples shown in Figure 1. Because of the uniformity of the particle size and shape, we anticipate that the electrocatalytic activity of these six samples of nanoparticles for formic acid oxidation can then be directly correlated to the particle composition.

Cyclic Voltammetry of $Fe_xPt_{100−x}$ Nanoparticles. As discussed in our previous report,[26] in order to render the FePt alloy particles electrochemically active, all the FePt particles modified Au electrodes were treated in UVO for 15 min to remove the organic protecting ligands. Figure 2 shows the steady-state cyclic voltammograms (CV) of the resulting $Fe_xPt_{100−x}$ ($x = 10, 15, 42, 54, 58,$ and 63) nanoparticles deposited onto a Au electrode in 0.1 M $HClO_4$ at a potential sweep rate of 0.1 V/s. It should be noted that Pt-based metal alloys usually exhibit the formation of a platinum skin after electrochemical cycling in acidic electrolytes, which is caused by the Pt dissolution from the alloy and then redeposition and rearrangement on the surface.[29−33]

Figure 1. Representative TEM micrographs of the series of FePt nanoparticles used in this study: (A) $Fe_{10}Pt_{90}$, (B) $Fe_{15}Pt_{85}$, (C) $Fe_{42}Pt_{58}$, (D) $Fe_{54}Pt_{46}$, (E) $Fe_{58}Pt_{42}$, and (F) $Fe_{63}Pt_{37}$. The scale bars are all 20 nm. The inset shows the corresponding particle core size histogram.

From Figure 2, it can be seen that the voltammetric features of all the Fe_xPt_{100-x}/Au electrodes are similar to those at a polycrystalline Pt electrode, suggesting the formation of a Pt skin on the alloy nanoparticle surface after electrochemical activation in 0.1 M $HClO_4$. First, the characteristic features for

hydrogen adsorption−desorption at low electrode potentials can be clearly observed. For instance, for the $Fe_{42}Pt_{58}$/Au electrode, one can see two pairs of well-defined current peaks at −0.43 and −0.31 V for hydrogen adsorption−desorption. Pt oxides are formed in the anodic scan at potentials above +0.3 V. In the

Table 1. Average Core Size, Size Distribution, and Composition of the Fe_xPt_{100-x} Nanoparticles

particle	A	B	C	D	E	F
core size (nm)[a]	2.44 ± 0.70	2.47 ± 0.56	2.35 ± 0.18	2.52 ± 0.81	2.48 ± 0.38	2.42 ± 0.61
core composition[b]	$Fe_{10}Pt_{90}$	$Fe_{15}Pt_{85}$	$Fe_{42}Pt_{58}$	$Fe_{54}Pt_{46}$	$Fe_{58}Pt_{42}$	$Fe_{63}Pt_{37}$

[a] Particle core sizes were derived from TEM images as exemplified in Figure 1. [b] Particle core compositions were evaluated by energy-dispersive X-ray analysis (EDX spectra are included in the Supporting Information, Figure S2).
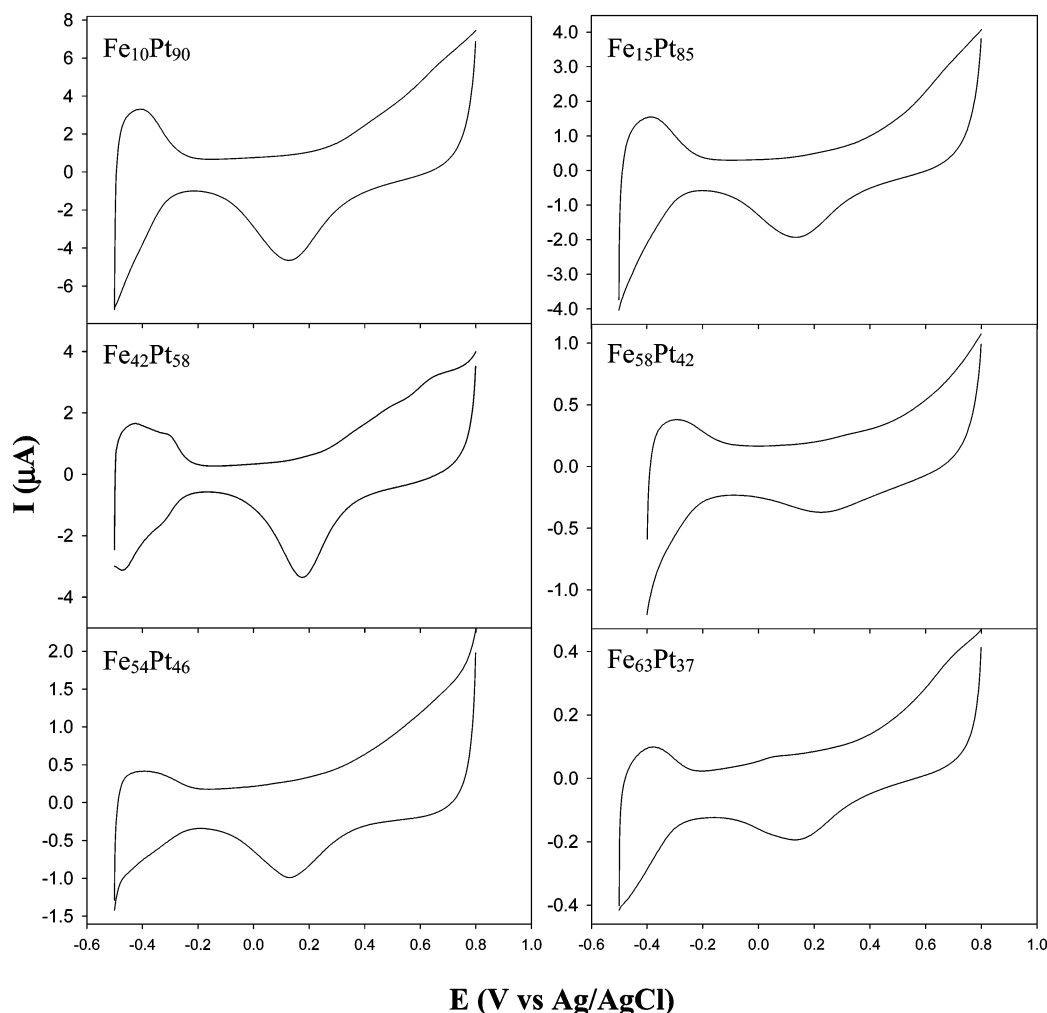
Figure 2. Cyclic voltammograms of the Fe_xPt_{100-x}/Au electrodes in 0.1 M $HClO_4$. The potential scan rates were 0.1 V/s.

reverse scan, a voltammetric peak for the reduction of Pt oxides can be observed at about +0.17 V. Similar responses can be seen with all other alloy particles, except for a broad and featureless hydrogen adsorption—desorption region. Second, by comparing the CV profiles of the Fe_xPt_{100-x} nanoparticles, it can be seen that the peak currents for the reduction of Pt oxides and for hydrogen adsorption—desorption become more prominent for the alloy nanoparticles with a higher Pt content, indicating a larger/thicker Pt skin layer on the particle surface. These electrodes were then employed in the subsequent studies of electro-oxidation of formic acid.

Electro-Oxidation of Formic Acid. Figure 3 depicts the steady-state cyclic voltammograms of formic acid oxidation at

the six Fe_xPt_{100-x}/Au electrodes prepared above. Note that the voltammetric currents have been normalized to the actual active surface areas of the respective electrodes which are calculated on the basis of the charge associated with hydrogen desorption (anodic current between −0.5 and −0.2 V in Figure 2), assuming that hydrogen desorption yields 210 $\mu C/cm^2$ of the Pt surface area.[34,35] It can be seen that the overall voltammetric behaviors are strongly dependent on the nanoparticle composition.

For the $Fe_{10}Pt_{90}$ nanoparticles, there are two voltammetric peaks at +0.083 and +0.378 V in the anodic scan, similar to the voltammetric features of HCOOH oxidation at $Fe_{20}Pt_{80}$ nanoparticle modified electrodes.[26,27] The first oxidation peak (E_{P1} = +0.083 V) is attributed to the direct oxidation of formic acid into CO_2 on the particle surface that is free of adsorbed poisonous intermediates (e.g., CO), i.e., the direct path, whereas the second peak at a more positive potential (E_{P2} = +0.378 V) is ascribed to the oxidation of CO species adsorbed on the particle surface that arise from the nonfaradaic dissociation of formic acid (the

(29) Toda, T.; Igarashi, H.; Uchida, H.; Watanabe, M. *J. Electrochem. Soc.* **1999**, *146*, 3750−3756.

(30) Watanabe, M.; Tsurumi, K.; Mizukami, T.; Nakamura, T.; Stonehart, P. *J. Electrochem. Soc.* **1994**, *141*, 2659−2668.
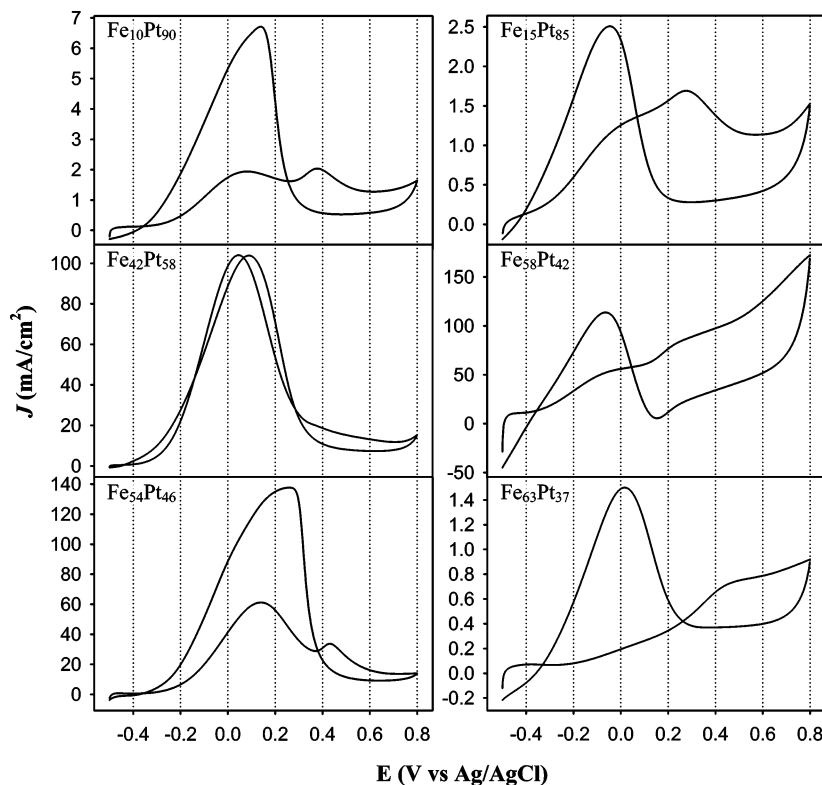
(31) Igarashi, H.; Fujino, T.; Zhu, Y. M.; Uchida, H.; Watanabe, M. *Phys. Chem. Chem. Phys.* **2001**, *3*, 306−314.

(32) Wan, L. J.; Moriyama, T.; Ito, M.; Uchida, H.; Watanabe, M. *Chem. Commun.* **2002**, 58−59.

(33) Xu, Y.; Ruban, A. V.; Mavrikakis, M. *J. Am. Chem. Soc.* **2004**, *126*, 4717−4725.

(34) Ye, H. C.; Crooks, R. M. *J. Am. Chem. Soc.* **2007**, *129*, 3627−3633.

(35) Stamenkovic, V. R.; Mun, B. S.; Arenz, M.; Mayrhofer, K. J. J.; Lucas, C. A.; Wang, G. F.; Ross, P. N.; Markovic, N. M. *Nat. Mater.* **2007**, *6*, 241−247.

Figure 3. Cyclic voltammograms of the Fe_xPt_{100-x}/Au electrodes in 0.1 M HCOOH + 0.1 M HClO$_4$. The potential scan rates were 0.1 V/s.

so-called indirect path). Additional current contributions may come from the direct oxidation of formic acid at the recovered particle surface upon CO oxidation. In the cathodic scan, an oxidation peak at +0.14 V is observed which is assigned to the direct oxidation of formic acid with the entire catalyst surface free of CO poisoning.

Thus, one can see that the ratio of the current density of the first anodic peak (J_a) to the cathodic peak (J_c) essentially reflects the fraction of the catalyst surface that is not poisoned by CO adsorption and can be used to measure the catalyst tolerance to CO poisoning. For the $Fe_{10}Pt_{90}$ nanoparticles, the J_a/J_c ratio is 0.29, suggesting that initially about 70% of the catalyst surface was poisoned by CO adsorption. Similar voltammetric behaviors can also be observed with $Fe_{58}Pt_{42}$, $Fe_{54}Pt_{46}$, and $Fe_{15}Pt_{85}$ nanoparticles. The corresponding J_a/J_c ratios are found to be 0.42, 0.47, and 0.52, respectively, indicative of reduced CO poisoning as compared to the $Fe_{10}Pt_{90}$ particles.

In contrast, the $Fe_{42}Pt_{58}$ and $Fe_{63}Pt_{37}$ particles exhibit drastically different voltammetric responses (Figure 3). For the low-platinum $Fe_{63}Pt_{37}$ particles, only one anodic peak is observed at +0.40 V, whereas the oxidation peak in the cathodic scan appears at +0.017 V, implying extensive poisoning of the catalyst surface by CO adsorption and, hence, a very low J_a/J_c ratio (0.17).

For the $Fe_{42}Pt_{58}$ nanoparticles, an opposite behavior can be seen (Figure 3). Here the voltammetric responses of HCOOH oxidation also show only one oxidation current peak in the anodic and cathodic scan. However, in comparison to those of the Fe_{10}-Pt_{90} particles, the peak potentials shift cathodically to +0.045 and +0.088 V in the anodic and cathodic scan, respectively, suggesting much enhanced electrocatalytic activities. More importantly, the absence of a second anodic peak at a more positive potential indicates little CO generation/adsorption during formic acid electro-oxidation. Such excellent tolerance to CO adsorption is further confirmed by the observation that the current density of the oxidation peak in the anodic scan is almost equal to that in the cathodic scan, with a corresponding J_a/J_c ratio close
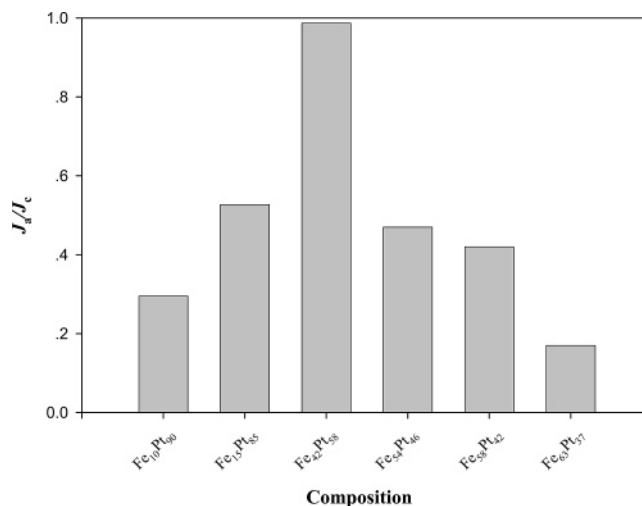

Figure 4. Ratio of the anodic and cathodic peak currents for the direct oxidation of formic acid at varied nanoparticle composition. The results were obtained from data presented in Figure 3.

to 0.99. This implies that the voltammetric currents mostly arise from the direct oxidation of formic acid into CO$_2$.

Figure 4 summarizes the J_a/J_c ratios of the six Fe_xPt_{100-x} alloy particles under study which clearly exhibit a peak-shaped variation with particle compositions. It is apparent that the $Fe_{42}Pt_{58}$ particles represent the optimum composition among the group of alloy catalysts. For alloy particles with too high or low a platinum content (e.g., $Fe_{10}Pt_{90}$, and $Fe_{63}Pt_{37}$), extensive CO poisoning occurs leading to minimum catalytic activities.

Similar assessments of the electrocatalytic activities can be made by the comparison of the anodic current density as well as the onset potential. For instance, from Figure 3 the current densities of the (first) anodic peak of the six Fe_xPt_{100-x} alloy nanoparticles ($x = 10, 15, 42, 54, 58,$ and 63) can be estimated to be 1.94, 1.32, 104.02, 61.18, 42.22, and 0.21 mA/cm^2,
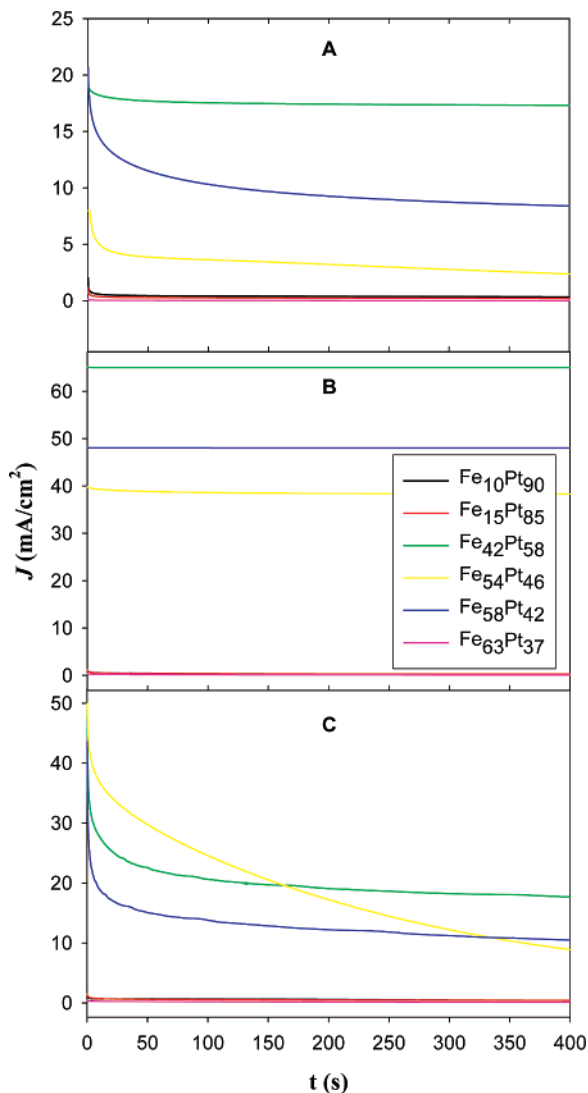
Figure 5. Chronoamperometric curves in 0.1 M HCOOH + 0.1 M HClO$_4$ for different Fe$_x$Pt$_{100-x}$/Au electrodes (shown in the figure legends) where the potential was stepped from E_i = −0.4 V to E_f = −0.02 (A), +0.05 (B), and +0.20 V (C).

respectively. Of these, the Fe$_{42}$Pt$_{58}$ particles exhibit the highest current density. In addition, the onset potentials for formic acid oxidation can be found at −0.33, −0.37, −0.40, −0.34, −0.39, and −0.25 V, respectively. Again, Fe$_{42}$Pt$_{58}$ stands out with the most negative onset potential for formic acid oxidation among the series.

To further evaluate the activity and stability of the Fe$_x$Pt$_{100-x}$ catalysts for formic acid oxidation, chronoamperometric analyses were also carried out by stepping the potential from E_i = −0.40 V to E_f = −0.20, +0.05, and +0.20 V in 0.1 M HCOOH + 0.1 M HClO$_4$, which corresponds, respectively, to the onset, peak, and end of the formic acid direct oxidation at the catalytic sites that are not poisoned by CO intermediates, as shown in Figure 5A−C. From the chronoamperometric curves at E_f = −0.20 V (Figure 5A), one can see that the maximum initial and steady-state oxidation current density was obtained with the Fe$_{42}$Pt$_{58}$/Au electrode followed by Fe$_{58}$Pt$_{42}$/Au and Fe$_{54}$Pt$_{46}$/Au, and the oxidation current density at the Fe$_{15}$Pt$_{85}$, Fe$_{10}$Pt$_{90}$ and Fe$_{63}$Pt$_{37}$ electrodes is much smaller. At E_f = +0.05 V (Figure 5B), which corresponds to the voltammetric peak in the CV studies of formic acid oxidation (Figure 3), again the Fe$_{42}$Pt$_{58}$/Au electrode shows the highest oxidation current density, and the electrodes exhibit the same activity and stability sequence as that at E_f = −0.2 V.
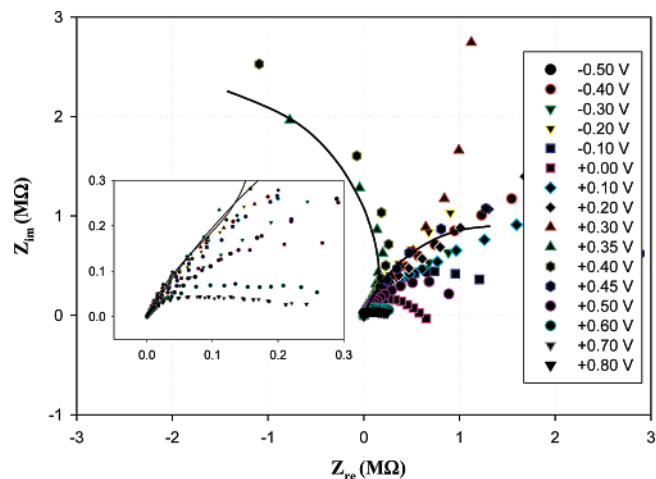
Figure 6. Complex-plane (Nyquist) impedance plots of the Fe$_{10}$-Pt$_{90}$/Au electrode in 0.1 M HCOOH + 0.1 M HClO$_4$ at various electrode potentials. The lines are representative simulations based on the equivalent circuits in Figure 9 for the impedance data at the electrode potentials of −0.4 and +0.35 V. The inset is the magnification of the impedance spectra in a smaller range.

For chronoamperometric curves at E_f = +0.20 V (Figure 5C), whereas the Fe$_{54}$Pt$_{46}$/Au electrode exhibits a higher initial oxidation current density than that on the Fe$_{42}$Pt$_{58}$/Au electrode, the current density decays rapidly. In contrast, the Fe$_{42}$Pt$_{58}$/Au electrode maintains a rather steady current profile, and at t > 150 s, the current density becomes the largest among the series. These chronoamperometric data indicate that Fe$_{42}$Pt$_{58}$ has the best activity and stability for formic acid oxidation among the series of Fe$_x$Pt$_{100-x}$ particles used in the present study, in good agreement with the CV results.

On the basis of the above CV and chronoamperometric evaluations, it can be seen that the catalytic activity decreases in the sequence of Fe$_{42}$Pt$_{58}$ > Fe$_{54}$Pt$_{46}$ ≈ Fe$_{58}$Pt$_{42}$ > Fe$_{15}$Pt$_{85}$ > Fe$_{10}$Pt$_{90}$ > Fe$_{63}$Pt$_{37}$. That is, the Fe$_x$Pt$_{100-x}$ particles at x ≈ 50 show the highest electrocatalytic activity in HCOOH oxidation among the series. For Pt-based bimetallic alloy electrocatalysts, the optimum composition should maximize the adsorption of HCOOH on the Pt active sites and, concurrently, there should be enough surface sites of the second metals which promote the effective oxidative removal of poisonous intermediates (e.g., CO) with adsorbed hydroxyl species.[18,36,37] For the Fe$_x$Pt$_{100-x}$ alloy particles in the present study, the optimum composition appears to correspond to a Fe/Pt atomic ratio of ca. 1:1, which is very similar to the PtRu catalysts used in previous investigations.[20,21]

Electrochemical Impedance Studies. Electrochemical impedance spectroscopy has been used as a powerful and sensitive technique to study the kinetics of electron-transfer processes. Here we carry out electrochemical impedance studies to examine the electro-oxidation dynamics of formic acid catalyzed by Fe$_x$Pt$_{100-x}$ alloy nanoparticles. Overall the EIS responses are very consistent with the respective voltammetric results as shown in Figures 3−5.
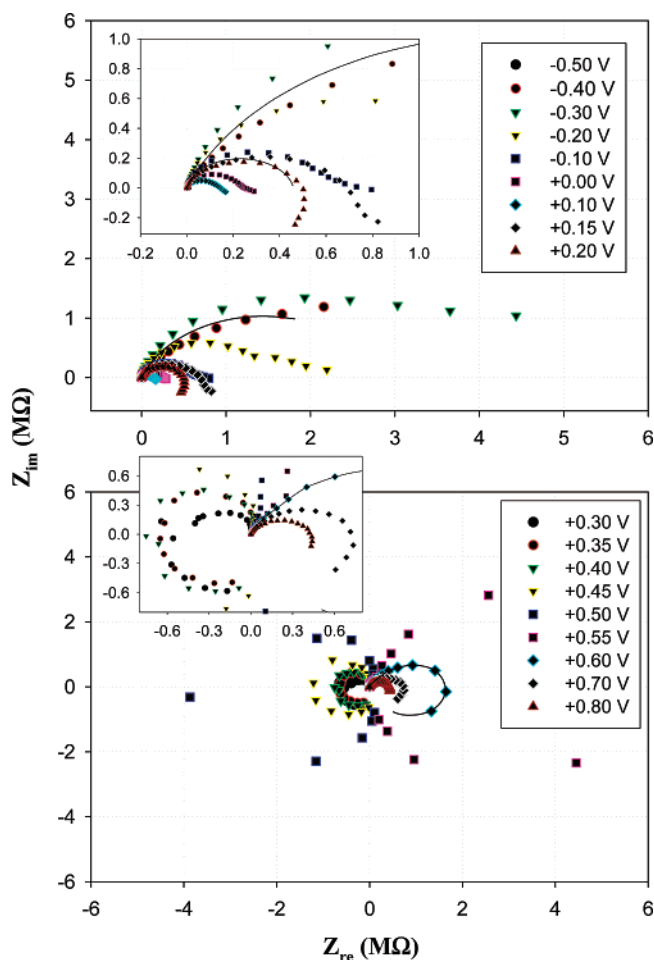
Figure 6 depicts the complex-plane (Nyquist) impedance plots of the Fe$_{10}$Pt$_{90}$/Au electrode in 0.1 M HCOOH + 0.1 M HClO$_4$ with electrode potentials varied from −0.50 to +0.80 V (shown as figure legends). It can be seen that, at potentials below +0.00 V, the impedance arcs are located within the first quadrant and the diameter of the arcs increases slightly from −0.50 to −0.20

(36) Watanabe, M.; Motoo, S. *J. Electroanal. Chem.* **1975**, *60*, 275−283.
(37) Kua, J.; Goddard, W. A. *J. Am. Chem. Soc.* **1999**, *121*, 10928−10941.

V and then decreases somewhat when the potential shifts positively from -0.20 to 0 V. The former may be ascribed to the formation and adsorption of CO intermediate species on the electrode surface, and the latter may be related to the onset of electro-oxidation of formic acid. With further increase of the electrode potentials ($+0.10$ to $+0.30$ V), the impedance arcs remain in the first quadrant, but the slope of the linear portions exhibit a rather rapid increase suggesting an increasingly dominant diffusion-controlled component because of the potential-enhanced electron-transfer kinetics. This agrees well with the voltammetric studies in Figure 3, as this potential region corresponds to the direct oxidation of formic acid at the catalytic sites that are not poisoned by CO adsorption. Additionally, the impedance arc starts to bend from the positive to negative direction of the x-axis at $+0.30$ V. When the electrode potential reaches $+0.35$ to $\sim +0.40$ V, the impedances actually appear in the second quadrant. The negative faradaic impedance suggests the presence of an inductive component. This is attributed to the formation of chemisorbed hydroxyl species in this potential range, which enhances the oxidative removal of the adsorbed CO intermediate, consistent with the voltammetric response (Figure 3) where a second anodic peak is observed. At more positive electrode potentials ($\geq +0.40$ V), the impedance arcs return to the first quadrant and the diameter of the arcs decreases with increasing potential, indicative of diminishing charge-transfer resistance. Overall, the impedance results are in very good agreement with voltammetric data presented above (Figure 3). Similar behaviors have been observed with the $Fe_{15}Pt_{85}$ and $Fe_{58}Pt_{42}$ alloy particles (Supporting Information), as well as with the $Fe_{20}Pt_{80}$ nanoparticles[26,27] that was reported previously.

Figure 7 shows the impedance spectra of the $Fe_{42}Pt_{58}$/Au electrode in 0.1 M HCOOH + 0.1 M HClO$_4$ at different electrode potentials. First, similarly, the impedance arcs are found mostly in the first quadrant (top panel), and the arc diameter first increases (from -0.50 to -0.30 V) and then decreases (from -0.30 to 0.10 V) with increasing electrode potential. The minimal arc diameter observed at $+0.1$ V appears to coincide with the voltammetric peak observed in Figure 3. With further increase of the electrode potential, the arc diameter increases correspondingly, and interestingly, the low-frequency ends of the arcs start to extend into the fourth quadrant ($+0.15$ to $+0.20$ V), indicating the presence of a small pseudoinductive component as a consequence of the oxidative removal of CO adsorbed on the particle surface. However, when the electrode potentials become more positive then $+0.30$ V (bottom panel), a drastic variation of the impedance spectra can be observed. First, the impedance spectra even show up in the second and third quadrants within the potential range of $+0.30$ to $+0.50$ V and then return to the first and fourth quadrants at higher potentials ($\geq +0.55$ V). Such interesting impedance patterns have also been reported in the studies of methanol electro-oxidation at Pt/C thin film electrodes.[38] They are ascribed to the variation of the rate-determining step at different potential positions, namely, the formation of adsorbed CO by dehydrogenation reaction of HCOOH and the electro-oxidation of adsorbed CO through adsorbed OH species. At potentials more negative than $+0.3$ V, the rate-determining step is considered to be the oxidation of adsorbed CO intermediates, leading to the appearance of the pseudoinductive behavior. At more positive potentials, the electro-oxidation of surface adsorbates will be drastically accelerated and the formation of

(38) Hsing, I. M.; Wang, X.; Leng, Y. J. *J. Electrochem. Soc.* **2002**, *149*, A615−A621.

Figure 7. Complex-plane (Nyquist) impedance plots of the Fe_{42}-Pt_{58}/Au electrode in 0.1 M HCOOH + 0.1 M HClO$_4$ at various electrode potentials. The lines are representative simulations based on the equivalent circuits in Figure 9 for the impedance data at the electrode potentials of -0.40 and $+0.60$ V. The insets are the magnification of the impedance spectra in a smaller range.

adsorbed CO by the dehydrogenation reaction of HCOOH now becomes the rate-determining step. This gives rise to the inductive response.[38]

In contrast, for the $Fe_{54}Pt_{46}$/Au electrode, all the impedance spectra are located in the first quadrant within the entire potential range of -0.50 to $+0.80$ V, as shown in Figure 8. This indicates that there exist only resistive behaviors for HCOOH electro-oxidation at the $Fe_{54}Pt_{46}$/Au electrode. The lack of (pseudo)-inductive characters of the impedance spectra seems to imply a relatively strong adsorption (and retarded oxidation kinetics) of CO on the particles surface, as voltammetric measurements (Figure 3) exhibit only a very weak current peak for the oxidation of adsorbed CO intermediates. In general, the impedance is rather comparable to that observed in Figure 6 for the $Fe_{10}Pt_{90}$ particles. Similar features are also observed with the low-platinum Fe_{63}-Pt_{37} nanoparticles (Supporting Information), except that the overall impedance is substantially larger.

The corresponding Bode plots of the impedance spectra for the series of Fe_xPt_{100-x} alloy particles are included in the Supporting Information. Overall, the characteristic frequency (f_{max}) at the maximum phase angle is found to increase with increasing electrode potentials, indicative of potential-enhanced electron-transfer kinetics. Additionally, within the potential range where surface-adsorbed CO is oxidized, an abrupt jump between the positive and negative values of the phase angle can be observed. This interesting behavior is attributed to the (pseudo)-
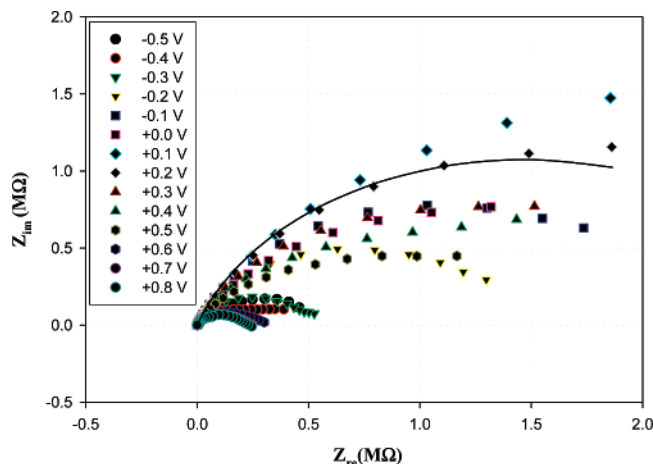
Figure 8. Complex-plane (Nyquist) impedance plots of the Fe_{54}-Pt_{46}/Au electrode in 0.1 M HCOOH + 0.1 M $HClO_4$ at various electrode potentials. The line is a representative simulation based on the equivalent circuits in Figure 9 for the impedance data at the electrode potential of +0.20 V.
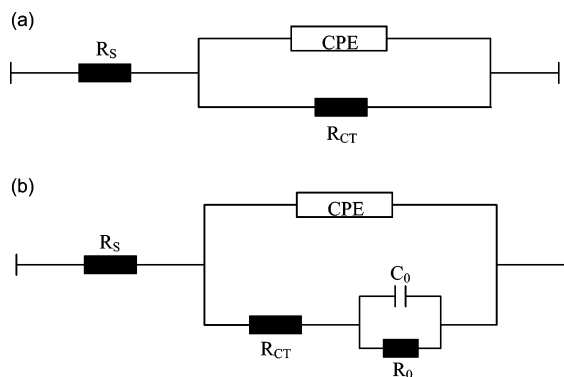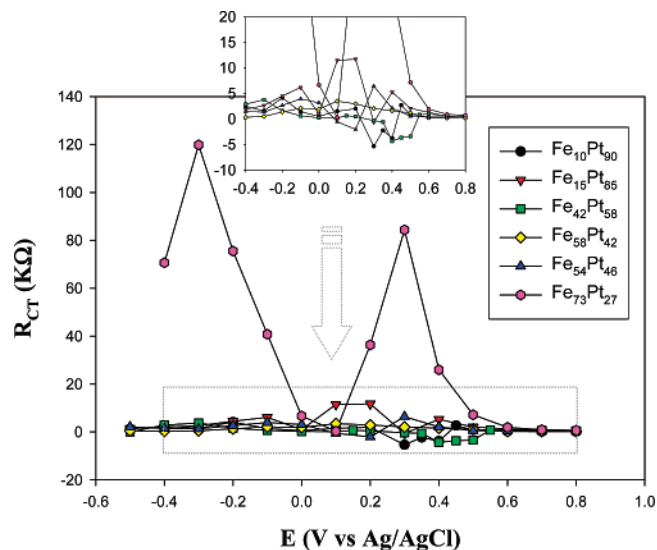

Figure 9. Equivalent circuits for the electro-oxidation of formic acid at Fe_xPt_{100-x}/Au electrodes.

inductive characteristics upon the oxidative removal of CO that gives rise to the negative faradaic impedance as shown in Figures 6−8.

On the basis of the above voltammetric and impedance measurements, two equivalent circuits are proposed in Figure 9, parts a and b, which are used to fit the impedance spectra corresponding to normal and negative impedance behaviors, respectively. Here R_S represents the solution resistance, CPE (constant-phase element) is the electrode double layer capacitance, R_{CT} is the charge-transfer resistance, and C_0 and R_0 represent the capacitance and resistance of the electro-oxidation of adsorbed CO intermediates, respectively. Some representative fittings are shown as solid lines in Figures 6−8, which show very good agreement with the corresponding experimental data.

Figure 10 depicts the variation of the charge-transfer resistance (R_{CT}) with the electrode potential for the series of Fe_xPt_{100-x} alloy nanoparticles. First, negative R_{CT} can be found within the potential range where (pseudo)inductive characters arise from the electro-oxidation of surface-adsorbed CO species. Second, the R_{CT} for formic acid oxidation at the $Fe_{42}Pt_{58}$/Au electrode appears to reach a minimum (a few hundred ohms) as compared to other alloy particles in the series (of the order of a few thousand ohms), again, confirming that this represents the optimum particle composition for formic acid electro-oxidation. Third, for Fe_{63}-Pt_{37} particles, the charge-transfer resistance (R_{CT}) is at least an order of magnitude greater than those of other particle catalysts, in agreement with the low electrocatalytic activities as shown in the voltammetric and impedance measurements.

Figure 10. Charge-transfer resistance (R_{CT}) at different electrode potentials. Data are obtained by curve fitting of the impedance spectra (Figures 6−8 and Supporting Information Figures S3−S5) by the equivalent circuits in Figure 9. The inset shows the magnification in a smaller range.

Conclusion

In this study, CV, chronoamperometry, and EIS were employed to examine the electrocatalytic activities of a series of Fe_xPt_{100-x} alloy nanoparticles ($x = 10, 15, 42, 54, 58,$ and 63) in the oxidation of formic acid in acid electrolytes. Three parameters in the CV studies were used as the indicators to evaluate the corresponding catalytic performance, including anodic oxidation current density, onset potential, as well as tolerance to CO poisoning. Our measurements suggest that the catalytic activity depends on the composition of the alloy nanoparticles, i.e., the catalytic activity decreases in the sequence of $Fe_{42}Pt_{58} > Fe_{54}Pt_{46} \approx Fe_{58}Pt_{42} > Fe_{15}Pt_{85} > Fe_{10}Pt_{90} > Fe_{63}Pt_{37}$. Consistent evaluation was observed in chronoamperometric measurements where the Fe_{42}-Pt_{58} particles exhibited the maximum current density and stability. In EIS measurements, for particles with excellent CO tolerance, negative impedance was observed at potentials where CO was removed by electro-oxidation, indicating the presence of an inductive component. However, for the nanoparticles heavily poisoned by CO, only normal impedance profiles were observed. These impedance measurements agree well with the CV results. Within the present experimental context, the Fe_xPt_{100-x} particles at $x \approx 50$ (i.e., the atomic ratio of Fe/Pt close to 1) represent the optimum alloy composition that exhibits the maximum anodic current density, most negative onset potential, and strongest tolerance to CO poisoning.

Supporting Information Available: UV−vis spectra, energy-dispersive X-ray analysis spectra (EDX), additional Nyquist plots, and Bode plots of the impedance spectra. This material is available free of charge via the Internet at http://pubs.acs.org.
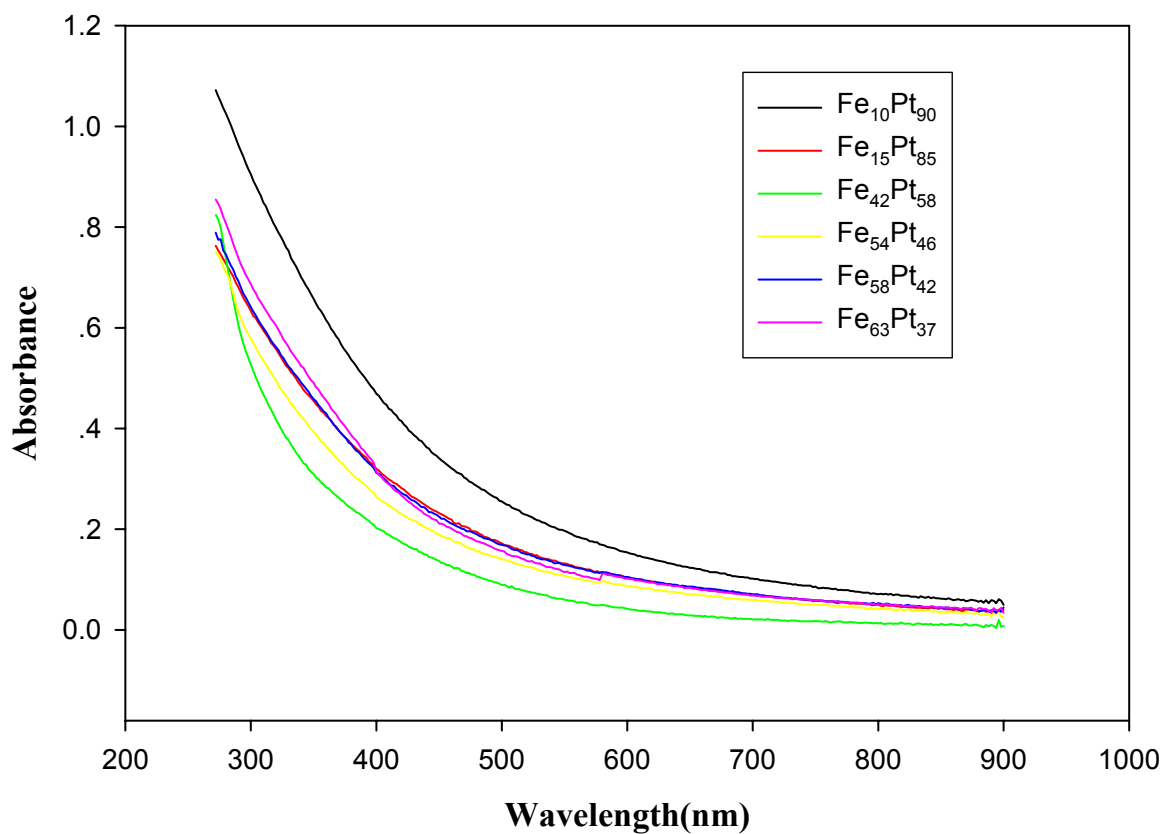
Composition Effect of FePt Bimetallic Nanoparticles on the Electro-oxidation

of Formic Acid

Wei Chen,[†] Jaemin Kim,[‡] Shouheng Sun,[‡] and Shaowei Chen[†*]

[†]Department of Chemistry and Biochemistry, University of California, Santa Cruz, California
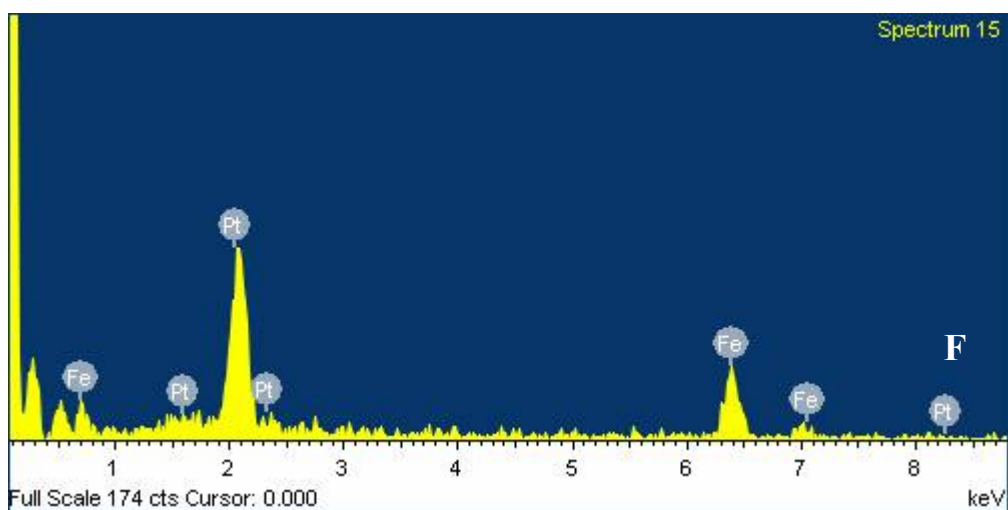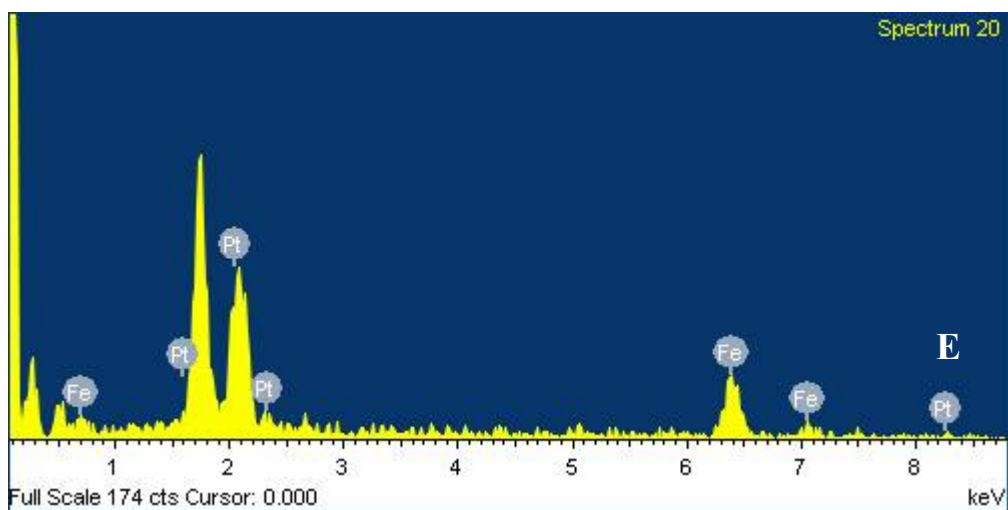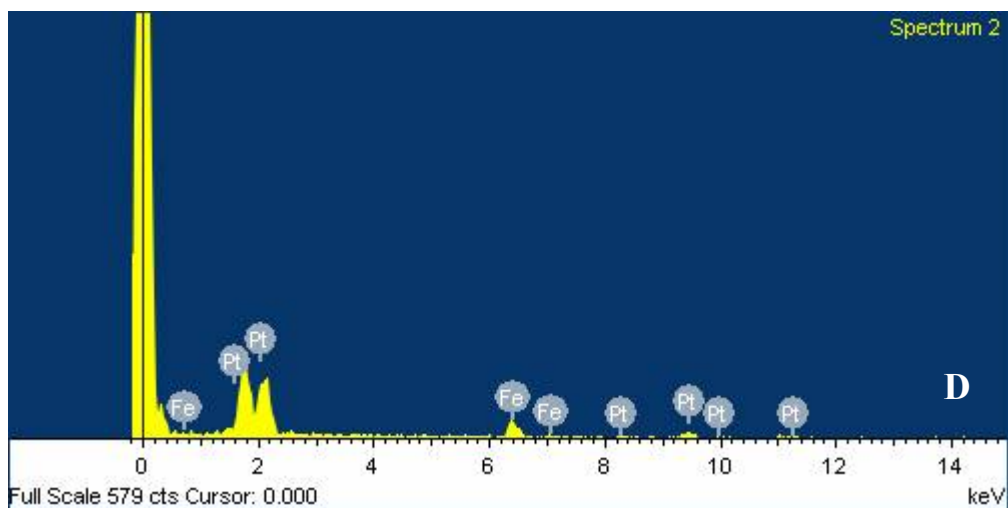
95064 USA

*[‡]Department of Chemistry, Brown University, Providence, Rhode Island 02912 USA*

Figure S1. UV-visible spectra of Fe_xPt_{100-x} nanoparticles (shown as figure legends). All the particle concentrations are 0.1 mg/mL in CH_2Cl_2.

---

[*] To whom all correspondence should be addressed. E-mail: schen@chemistry.ucsc.edu
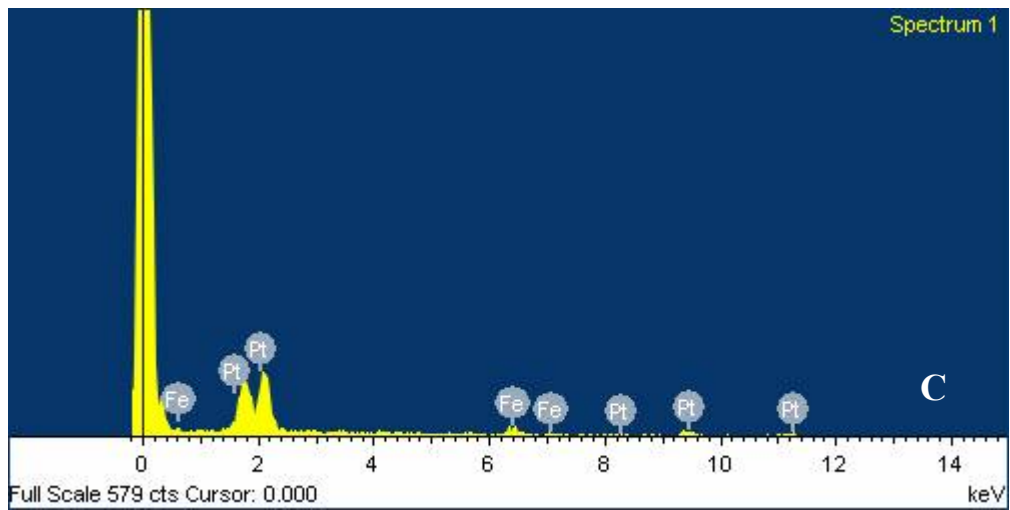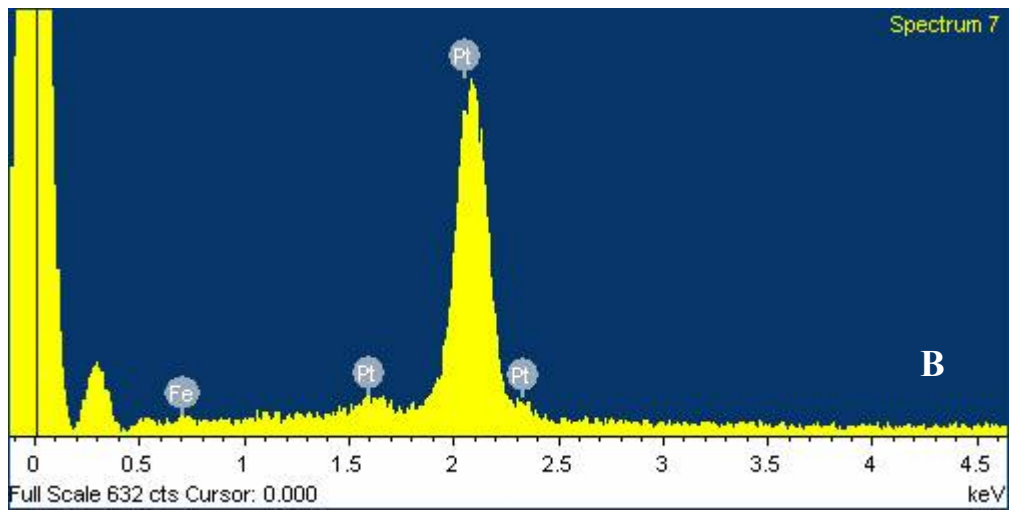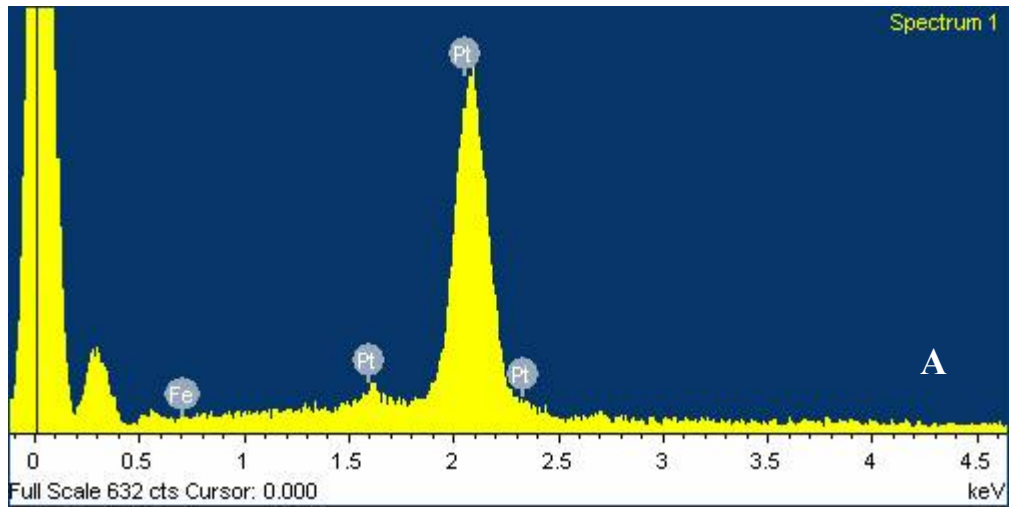
Figure S2. Energy-dispersive *x*-ray spectra of Fe$_x$Pt$_{100-x}$ nanoparticles: (A) Fe$_{10}$Pt$_{90}$; (B) Fe$_{15}$Pt$_{85}$; (C) Fe$_{42}$Pt$_{58}$; (D) Fe$_{54}$Pt$_{46}$; (E) Fe$_{58}$Pt$_{42}$; and (F) Fe$_{63}$Pt$_{37}$.
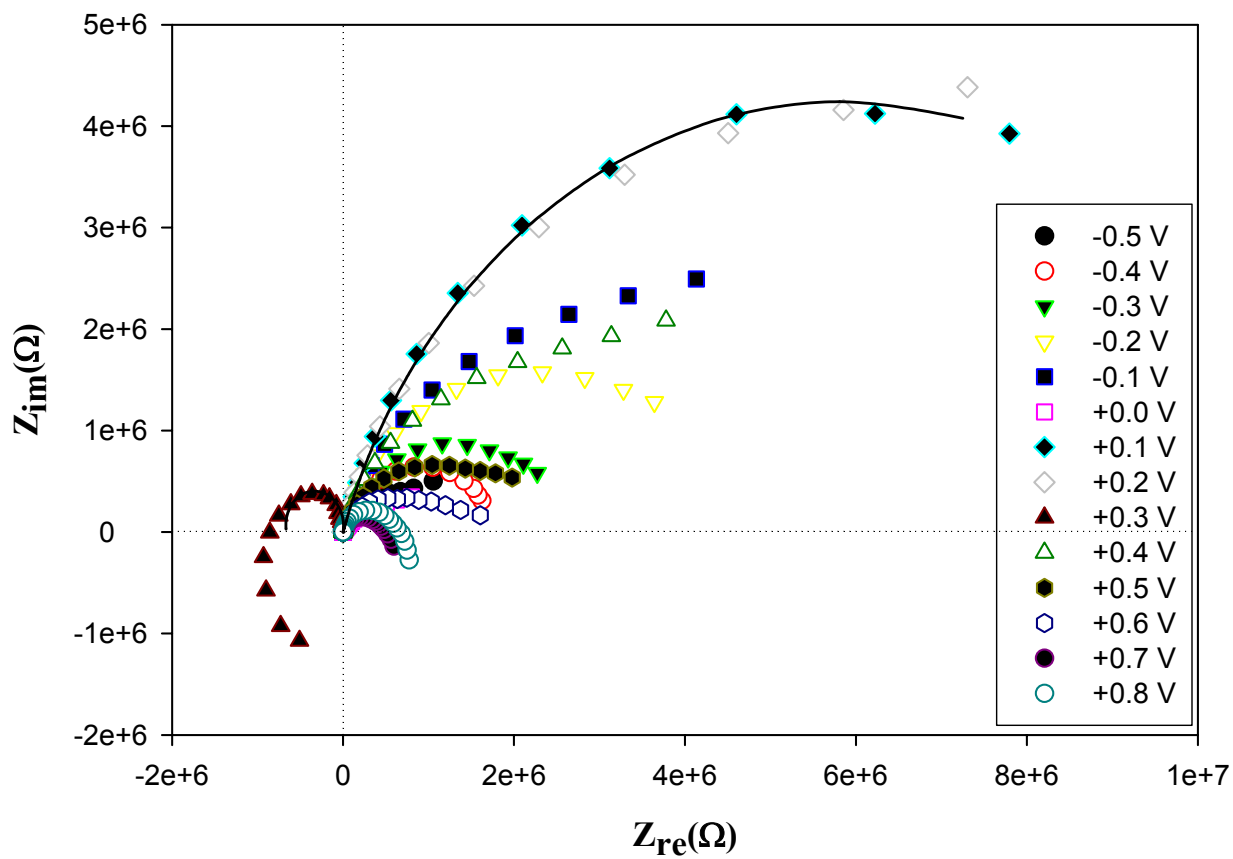
Figure S3. Complex-plane electrochemical impedance plots (Nyquist plots) of Fe$_{15}$Pt$_{85}$/Au electrode in 0.1 M HCOOH + 0.1 M HClO$_4$ at various electrode potentials. Line is a representative simulation based on the equivalent circuits in Figure 9 for the impedance data at the electrode potential of +0.10 V.
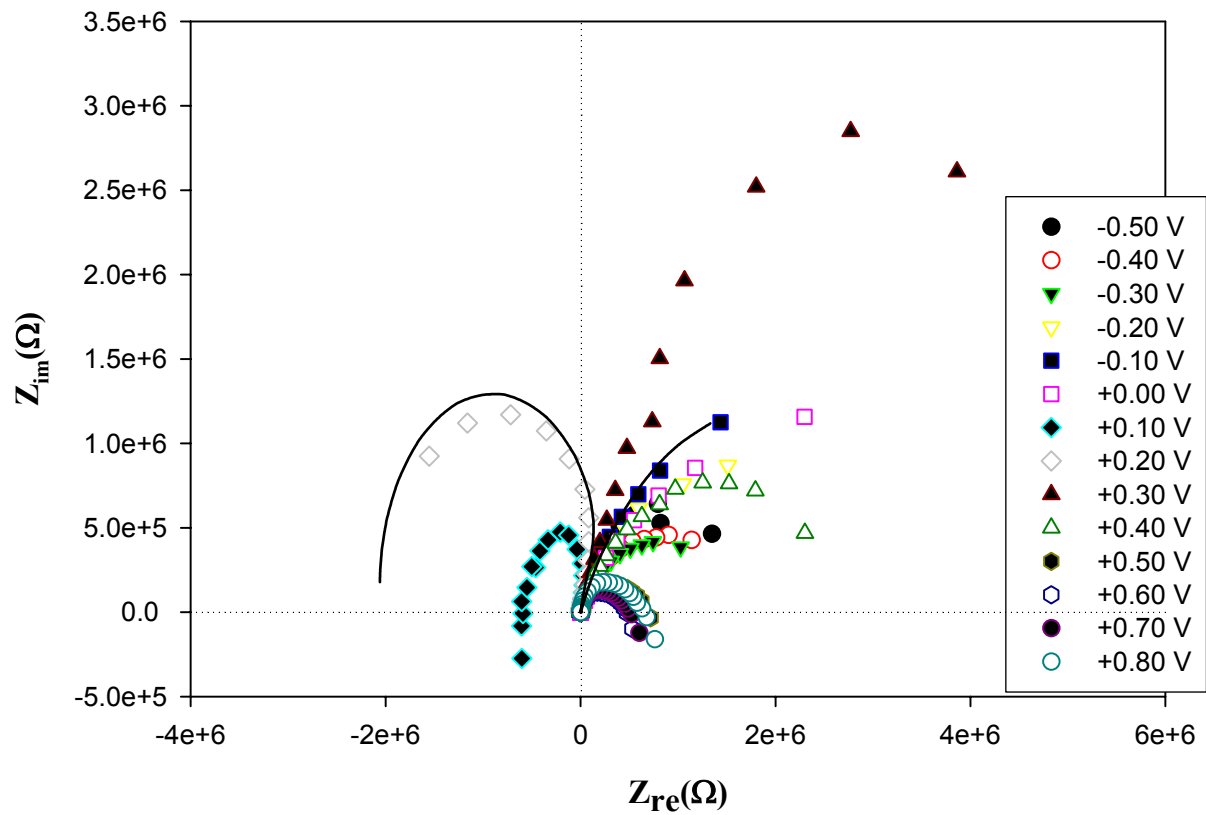
Figure S4. Complex-plane electrochemical impedance plots (Nyquist plots) of $Fe_{58}Pt_{42}/Au$ electrode in 0.1 M HCOOH + 0.1 M $HClO_4$ at various electrode potentials. Lines are representative simulations based on the equivalent circuits in Figure 9 for the impedance data at the electrode potentials of +0.10 and +0.2 V.
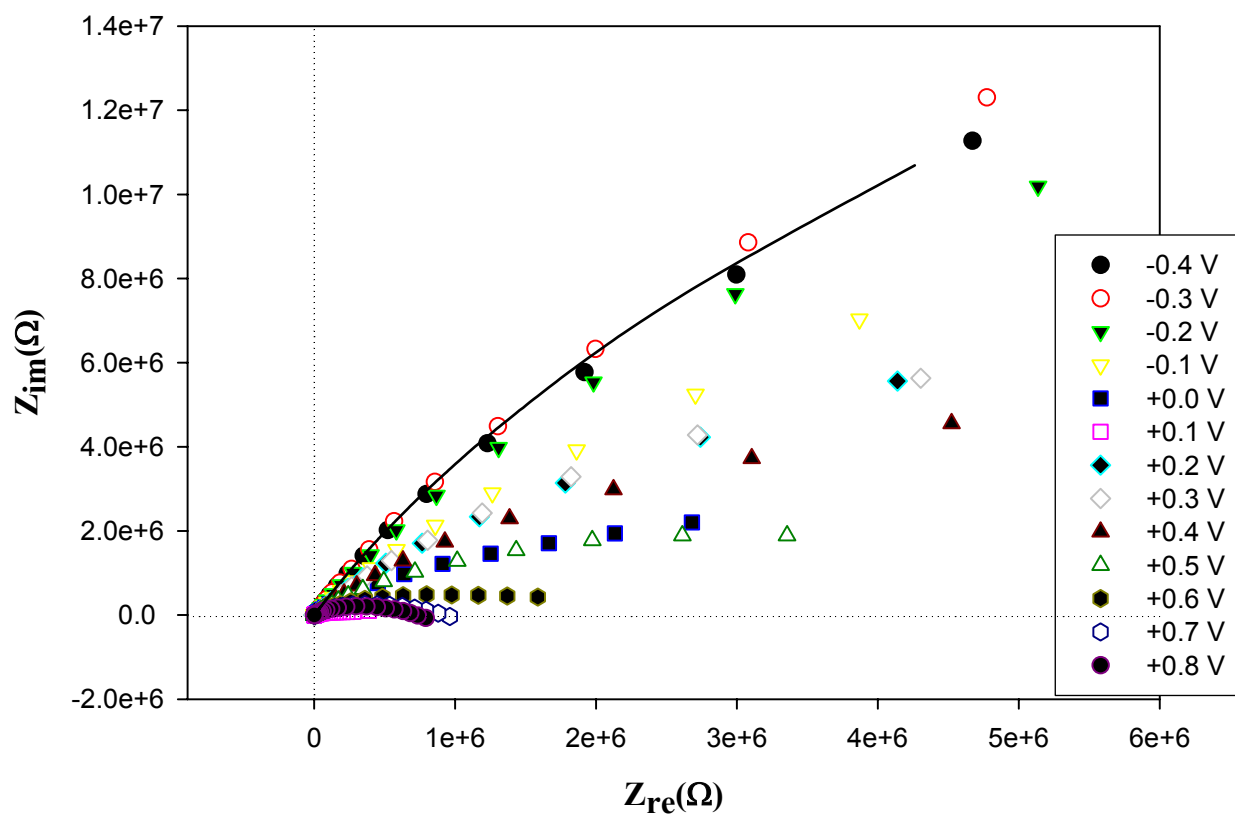
Figure S5. Complex-plane electrochemical impedance plots (Nyquist plots) of Fe_{63} Pt_{37}/Au electrode in 0.1 M HCOOH + 0.1 M $HClO_4$ at various electrode potentials. Line is a representative simulation based on the equivalent circuits in Figure 9 for the impedance data at the electrode potentials of –0.30 V.
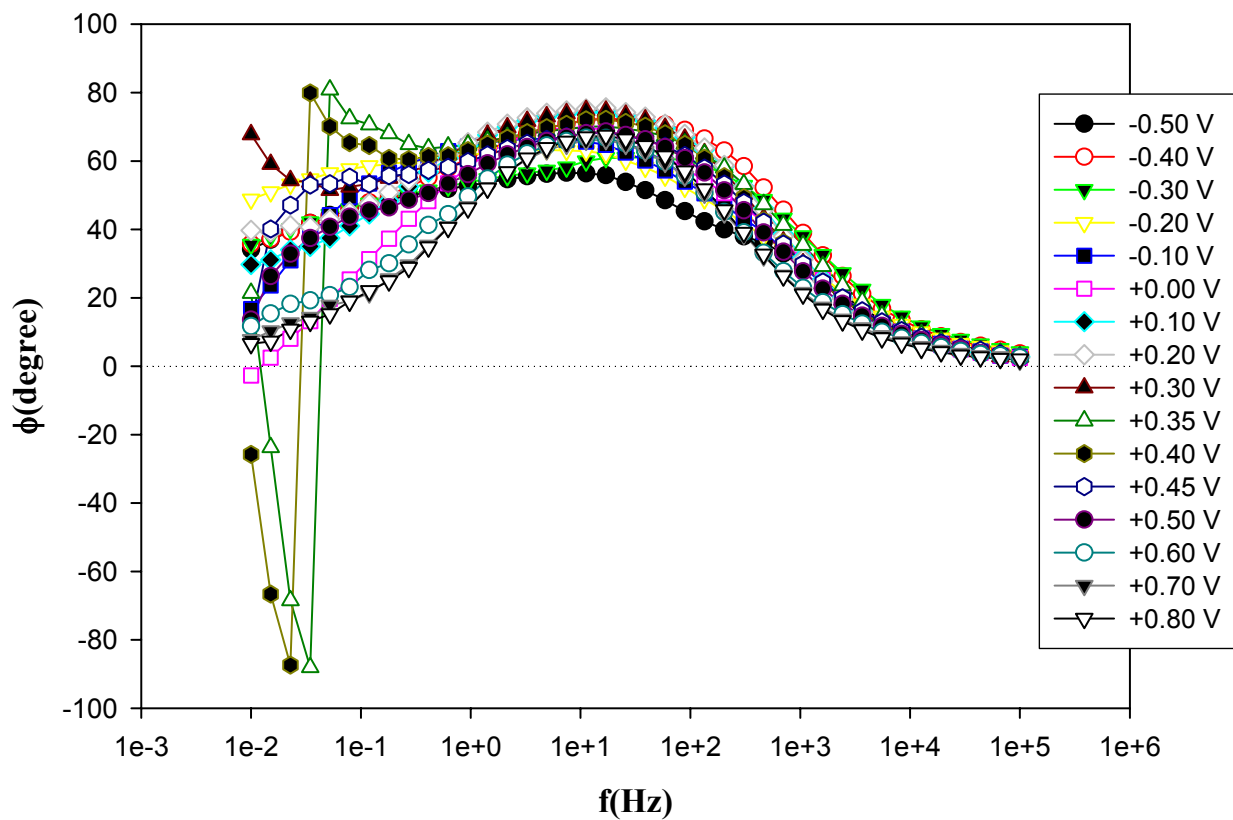
Figure S6. Bode plots of the electrochemical impedance of $Fe_{10}Pt_{90}/Au$ electrode in 0.1 M HCOOH + 0.1 M $HClO_4$ at various electrode potentials.
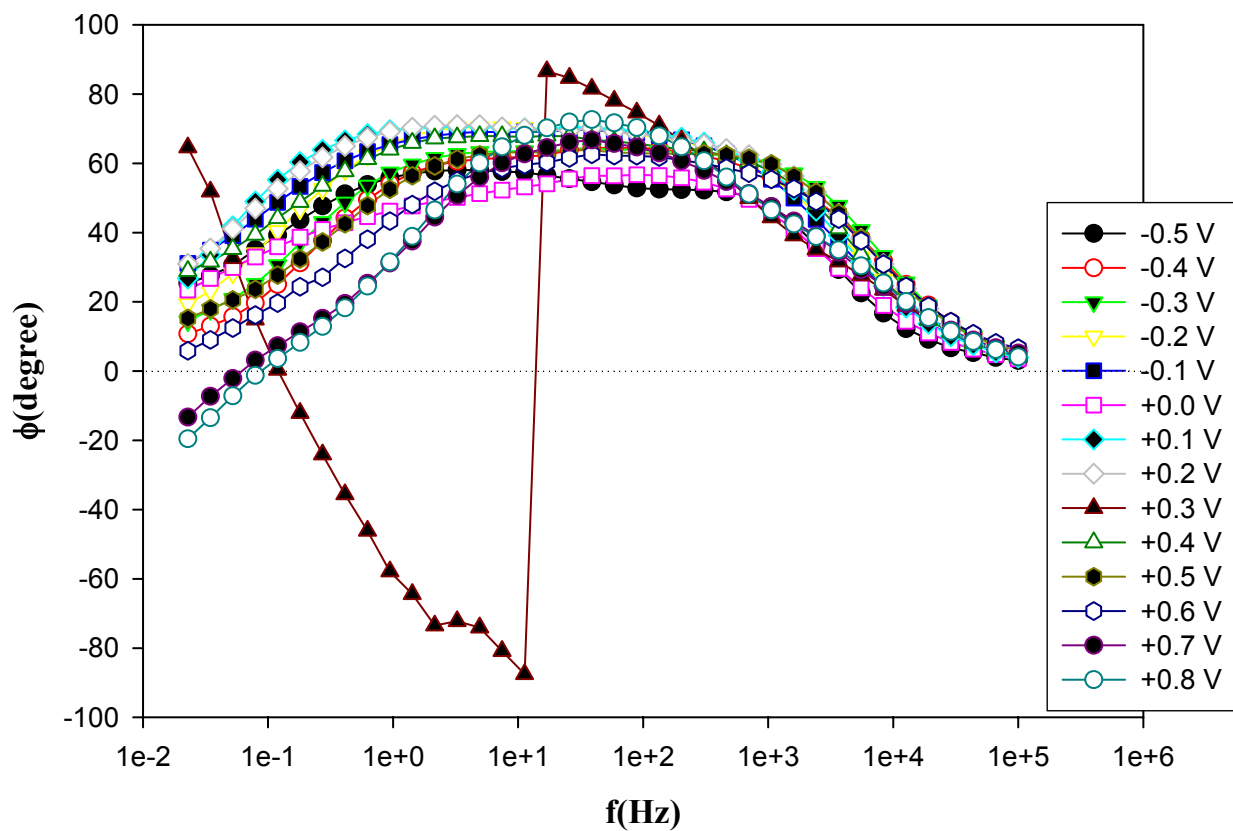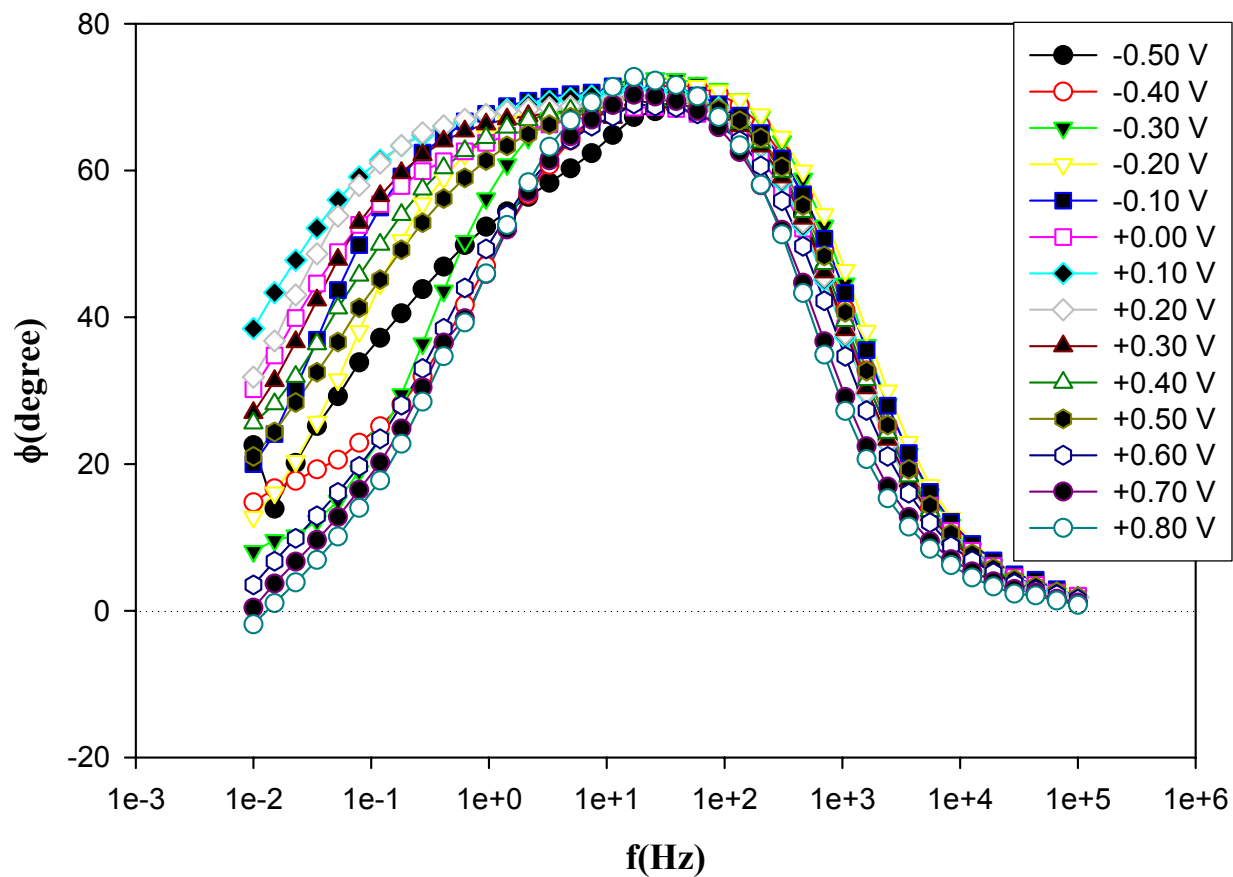
Figure S7. Bode plots of the electrochemical impedance of $Fe_{15}Pt_{85}$/Au electrode in 0.1 M HCOOH + 0.1 M $HClO_4$ at various electrode potentials.
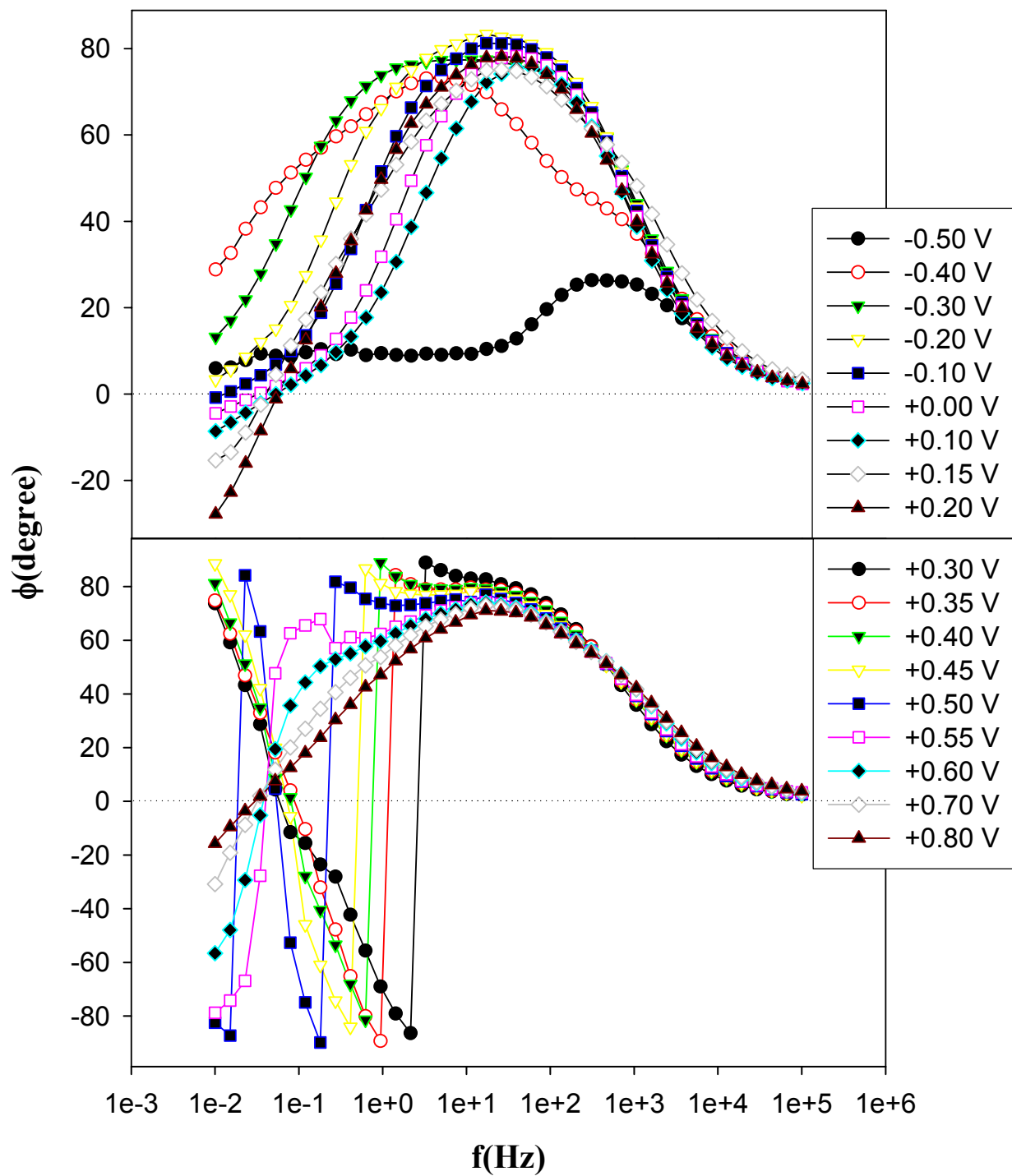
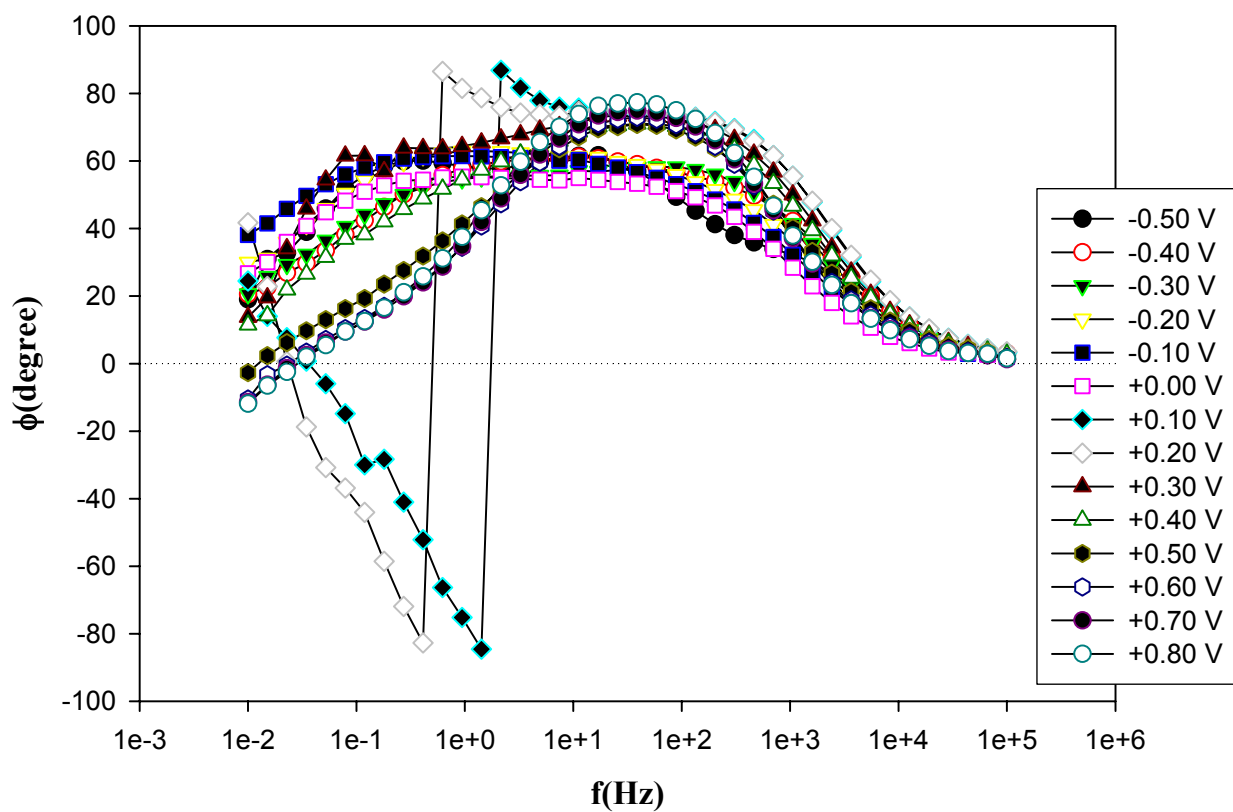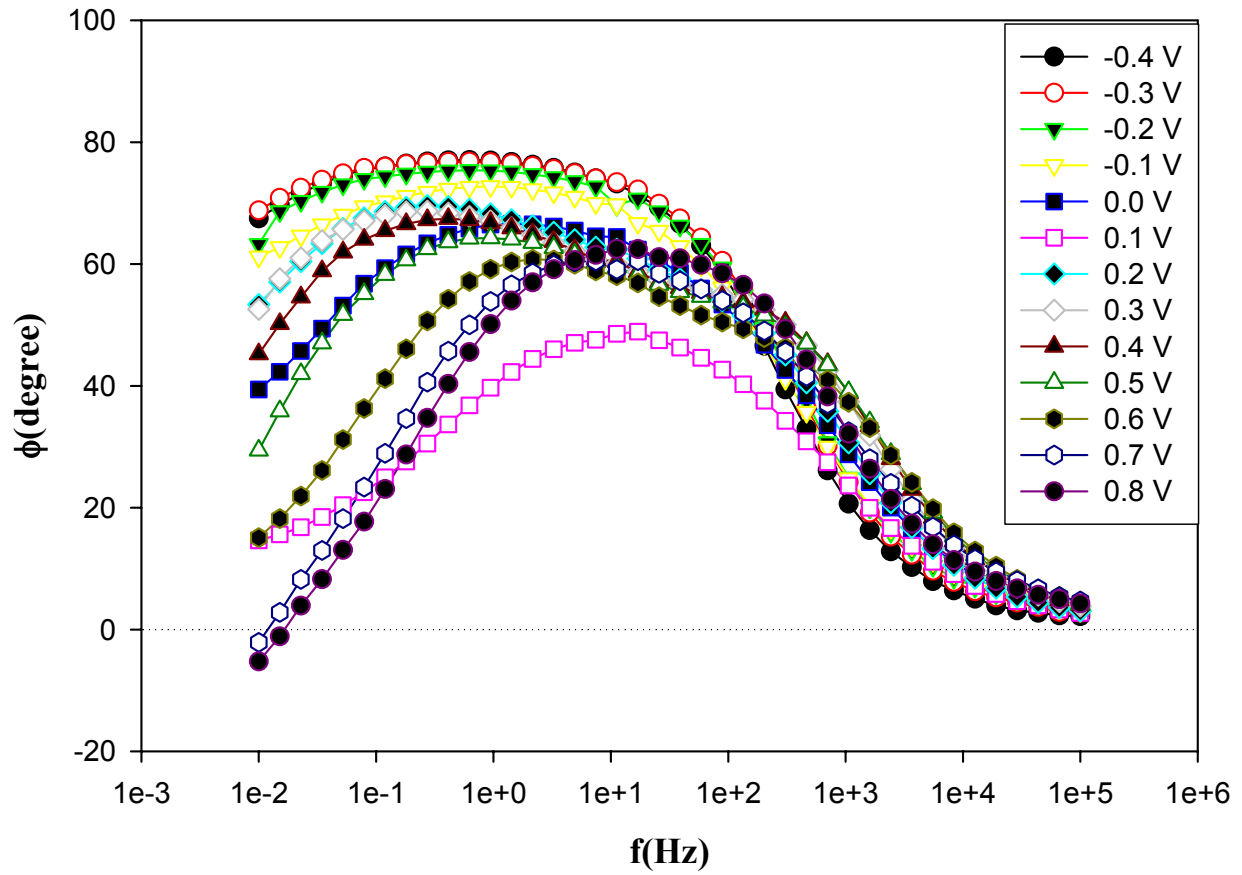**Figure S8.** Bode plots of the electrochemical impedance of $Fe_{42}Pt_{58}$/Au electrode in 0.1 M HCOOH + 0.1 M $HClO_4$ at various electrode potentials.

Figure S9. Bode plots of the electrochemical impedance of $Fe_{54}Pt_{46}/Au$ electrode in 0.1 M HCOOH + 0.1 M $HClO_4$ at various electrode potentials.

Figure S10. Bode plots of the electrochemical impedance of $Fe_{58}Pt_{42}/Au$ electrode in 0.1 M HCOOH + 0.1 M $HClO_4$ at various electrode potentials.

Figure S11. Bode plots of the electrochemical impedance of $Fe_{63}Pt_{37}/Au$ electrode in 0.1 M HCOOH + 0.1 M $HClO_4$ at various electrode potentials.